Experimental Thermal and Fluid Science 81 (2017) 382–395

Contents lists available at ScienceDirect

Experimental Thermal and Fluid Science

journal homepage: www.elsevier.com/locate/etfs

Integral turbulent scales in unsteady rapidly varied open channel flows

Xinqian Leng, Hubert Chanson *

The University of Queensland, School of Civil Engineering, Brisbane, QLD 4072, Australia

ARTICLE INFO

Article history:
Received 17 June 2016
Accepted 25 September 2016
Available online 28 September 2016

Keywords:
Integral turbulent time scales
Integral turbulent length scales
Unsteady open channel flows
Bores
Positive surges
Physical modelling

ABSTRACT

In an open channel, a rise in free surface elevation is called a positive surge and may occur in man-made channels as well as natural estuaries. Herein new unsteady velocity profiling measurements were performed in positive surges using a relatively large laboratory facility. An ensemble-averaged technique was applied by repeating 25 times each controlled flow condition. The velocity characteristics, Reynolds stress properties and integral turbulent scales were deduced to characterise the unsteady turbulence induced by the surge propagation. The profiling data indicated that the longitudinal velocity profile within the inner region of the turbulent boundary layer followed the log law before, during and after the surge passage. The integral turbulent time and length scale results indicated that the propagation of a positive surge generated an unsteady and anisotropic turbulence. Dimensionless turbulent time and length scale data yielded $L_{z,z}/L_{z,x} \sim 1.1$–7.3 and $T_{z,z}/T_{z,x} \sim 1.1$–14.4 for all the flow conditions, suggesting vortical structures with longer dimensions in the vertical direction compared to those in the horizontal directions.

© 2016 Elsevier Inc. All rights reserved.

1. Introduction

In an open channel, steady flow conditions may be achieved when the discharge and boundary conditions remain constant for a reasonable period of time. The operation of a regulation device, e.g. a gate, induces some unsteady flow motion in both upstream and downstream directions [9,31,12]. Unsteady open channel flows may be analysed using the Saint-Venant equations and the method of characteristics in channels of relatively simple geometry. The Saint-Venant equations describe the variations with time of the water depth d and flow velocity V:

$$B \times \frac{\partial d}{\partial t} + A \times \frac{\partial V}{\partial x} + B \times V \times \frac{\partial d}{\partial x} + V \times \left(\frac{\partial A}{\partial x}\right)_{d=\text{constant}} = 0 \quad (1)$$

$$\frac{\partial V}{\partial t} + V \times \frac{\partial V}{\partial x} = -g \times \frac{\partial d}{\partial x} + g \times (S_o - S_f) \quad (2)$$

where x is the longitudinal co-ordinate positive downstream, A is the flow cross-section area, B is the free-surface width, g is the gravity acceleration, S_o is the bed slope and S_f is the friction slope [20,2]. A rise in water surface elevation is called a positive surge [9,12]. It may occur in man-made channels [1] while a geophysical application is a tidal bore [32] (Fig. 1). The leading edge of the surge is characterised by a sudden discontinuity in water depth associated with a major redistribution of the velocity and pressure field [13,17]. The surge front is defined by its Froude number Fr_1, whose expression may be derived based upon momentum considerations for an irregular channel cross-section:

$$Fr_1 = \frac{V_1 + U}{\sqrt{g \times \frac{A_1}{B_1}}} \quad (3)$$

where V_1 is the initial flow velocity positive downstream, U is the surge celerity positive upstream, g is the gravity acceleration, and the subscript 1 refers to the initial flow conditions [4]. For a Froude number less than 1.3–1.4, the surge is undular [23,1]. For $Fr_1 > 1.4$, the surge has a breaking roller [13,6].

Herein, new unsteady velocity profiling measurements were performed systematically in positive surges. Using a relatively large laboratory facility, an ensemble-averaged technique was applied by repeating 25 times each controlled flow experiment. The velocity characteristics, Reynolds stress properties and integral turbulent scales were deduced to characterise the unsteady turbulence induced by the surge propagation.

2. Experimental facility, instrumentation and analyses

2.1. Physical facility and instrumentation

The experimental test section was 19 m long and 0.7 m wide, made of glass side walls and smooth flat PVC bed with adjustable

* Corresponding author.
E-mail address: h.chanson@uq.edu.au (H. Chanson).

http://dx.doi.org/10.1016/j.expthermflusci.2016.09.017
0894-1777/© 2016 Elsevier Inc. All rights reserved.

Fig. 1. Tidal bore of the Dordogne River (France) on 1 November 2015 between Luchey and Moulon (about 150 km upstream of the river mouth) - View from the left bank at late sunrise.

channel slope, previously used by Leng and Chanson [18]. The inflow was supplied by an upstream intake structure equipped with flow calming devices and flow straighteners, leading to the test section through a smooth three-dimensional convergent. The water discharge was measured by a magneto flow meter with an accuracy of 10^{-5} m^3/s, and checked against the brink depth at the downstream end of the flume. The positive surge was generated by rapidly closing a Tainter gate located next to the downstream end of the channel at x = 18.1 m, where x is measured from the upstream end of the channel, and the surge propagated upstream (Fig. 2A). A radial gate was located at x = 18.88 m to control the initial water depth.

In steady flows, the water depths were measured using point gauges with an accuracy of 0.001 m. The unsteady water elevations were recorded with a series of acoustic displacement meters Microsonic™ Mic + 35/IU/TC and Microsonic™ Mic + 25/IU/TC spaced along the channel between x = 1.75 m and x = 18.17 m. All acoustic displacement meters were calibrated against point gauge measurements in steady flows and the sensors were sampled at 100 Hz. The velocity measurements were performed with a Nortek™ acoustic Doppler velocimeter (ADV) Vectrino II Profiler (Serial number P27338, Hardware ID VNO 1366). The ADV Profiler had a fixed downward-looking head, equipped with a central emitter and four receivers, capable of recording velocity components simultaneously in 35 cells along a 35 mm profiling range. The velocity range was ±1.0 m/s and the sampling frequency was 100 Hz. The Profiler was located at x = 8.5 m, and the synchronisation between all instruments was within ±1 ms.

2.2. Signal processing and analyses

A series of velocity profiling measurements were conducted at different vertical elevations within the initial flow depth d_1, each profile covering a vertical range of 35 mm, with the upper point located 40 mm below the profiler emitter (Fig. 2B). In steady flows, the post-processing of ADV Profiler data included the removal of data with average correlation values less than 90% and average signal to noise ratio less than 5 dB. In addition, the phase-space thresholding technique developed by Goring and Nikora [10] was applied to removal spurious points in the data set. In the unsteady flows, the above post-processing technique was not applicable [22,17,3], and raw data was used.

An ensemble-averaged technique was applied: 25 experimental runs were repeated for each set of flow conditions, the number of repeats being determined based upon a sensitivity analysis [19]. The results were ensemble-averaged to obtain the median properties and associated fluctuations. Following Chanson and Docherty [6], the Reynolds stress components $\rho \times v_i \times v_j$ and stress fluctuations were calculated, with $v = V - \overline{V}$ where V is the instantaneous velocity measurement, v is the instantaneous velocity fluctuation, $\overline{V}$ is the ensemble-averaged median velocity, and i, j = x, y, or z. Both normal and tangential Reynolds stress components were analysed herein.

The turbulent time and length scales include the Eulerian integral time scale T_E, turbulent integral time scale $T_{z,i}$ and turbulent integral length scale $L_{z,i}$. The Eulerian integral time scale, also called auto-correlation time scale or macro time scale, is defined as:

$$T_{E,i} = \int_0^{\tau(R_{ii}=0)} R_{ii}(\tau) \times d\tau \tag{4}$$

where R_{ii} is the normalised auto-correlation function of the turbulent velocity fluctuation v_i, τ is the time lag, and $R_{ii}(\tau) = 0$ denotes the first crossing of the autocorrelation function with the x-axis. The Eulerian integral time scale $T_{E,i}$ is a measure of the longest connection in the turbulent behaviour of $v_i(\tau)$ [11,5]. In Eq. (4), $R_{ii}(\tau)$ is the normalised auto-correlation function of the i-velocity fluctuations for single point measurements defined as:

$$R_{ii}(\tau) = \frac{\overline{v_i(t) \times v_i(t+\tau)}}{\overline{v_i^2}} \tag{5}$$

with the auto-correlation function being unity for zero time lag and ranging between -1 and 1 for $\tau \neq 0$.The turbulent integral time and length scales were calculated based upon the cross-correlation of the instantaneous velocity signals between two points located at different elevations z_1 and z_2 on the vertical profile:

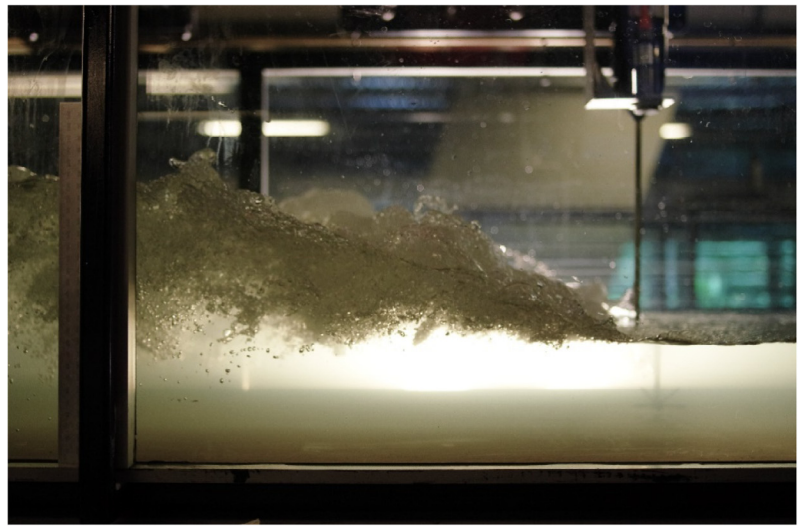

(A) Photograph of the breaking bore (Q = 0.102 m^3/s, Fr_1 = 2.3, shutter speed: 1/2,000 s)

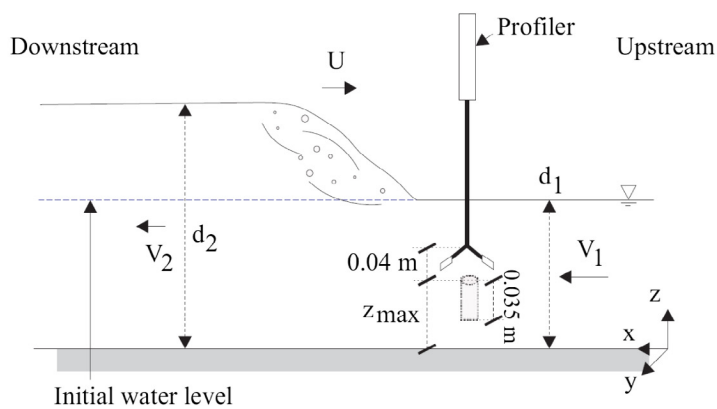

(B) Definition sketch of a propagating tidal bore and velocity profiler

Fig. 2. Positive surge propagation in rectangular prismatic channel - Bore propagation from left to right.

$$R_{z1z2,i}(\tau) = \frac{\overline{v_{z1,i}(t) \times v_{z2,i}(t+\tau)}}{\sqrt{\overline{v_{z1,i}^2} \times \overline{v_{z2,i}^2}}} \tag{6}$$

where $R_{z1z2,i}$ is the cross-correlation function in terms of the velocity component i. The turbulent integral length scale represents a characteristic vertical size of large vortical structure found in the velocity direction i, and it is defined as:

$$L_{z,i} = \int_0^{\Delta z_{max}} (R_{z1z2,i})_{max} \times dz \tag{7}$$

where $(R_{z1z2,i})_{max}$ is the peak of the cross-correlation function between the two points z_1 and z_2, and Δz_{max} is the maximum vertical separation between two points in a profile. The turbulent integral time scale characterises the lifespan of a large vortical motion detected in the velocity direction i and is defined as:

$$T_{z,i} = \frac{1}{L_{z,i}} \times \int_0^{\Delta z_{max}} (R_{z1z2}, i)_{max} \times T_{z1z2,i} \times dz \tag{8}$$

where $T_{z1z2,i}$ is the integral of the cross-correlation function between the time lag associated with the peak correlation and the first intersection of the function with zero.

2.3. Initial flow conditions

At x = 8.5 m, experimental data indicated that the initially-steady flow was partially developed and the dimensionless boundary layer thickness δ/d_1 was between 0.3 and 0.5. In the wall region, the vertical distribution of the time-averaged streamwise velocity V_x followed a logarithmic velocity law, also called the law of wall for a smooth turbulent boundary layer:

$$\frac{V_x}{V_*} = \frac{1}{\kappa} \times \mathrm{Ln}\left(\rho \times \frac{V_* \times z}{\mu}\right) + D_1 \quad 30 \text{ to } 70 < \rho \times \frac{V_* \times z}{\mu} \text{ and } \frac{z}{\delta} < 0.1 \text{ to } 0.2 \tag{9}$$

where V_* is the shear velocity: $V_* = (\tau_o/\rho)^{1/2}$, κ is the von Karman constant (κ = 0.4), τ_o is the boundary shear stress, z is the vertical elevation above the surface of the channel bed, ρ and μ are the fluid density and dynamic viscosity respectively, D_1 is an integration constant equal to 5 [27,24,5]. Present longitudinal velocity data are compared to the theoretical log law profile (Eq. (9)) in Fig. 3. In each case, the shear velocity was estimated from the best fit of the log law and reported in the figure caption. Fig. 3 presents profiles of time-averaged longitudinal velocity for a range of flow conditions and the data are compared to previous ADV measurements

[19] and the log law within the inner region. Overall, the majority of the inner region data followed the theoretical log law curve, except for the first four to five data points, corresponding to locations less than 5 mm from the bed.

In steady flows, the boundary friction τ_o may be estimated from the best fit of the log law and of longitudinal free-surface profile, and compared to the tangential Reynolds stress $\rho \times v_x \times v_z$ in the vicinity of the bed. Indeed, for vertical elevations immediately above the channel bed, the tangential Reynolds stress $\rho \times v_x \times v_z$ may be used to approximate the boundary shear stress [21]. The present results yielded boundary shear stress estimates of the same order of magnitude, with $V_*^2/V_1^2 \approx 0.0025$–$0.0075$ depending upon the flow conditions.

Outside of the boundary layer, the theoretical velocity distribution was a straight line: $V_x = V_{max}$. The free-stream velocity V_{max} was checked against the equation of conservation of mass:

$$q = \left(\left(\frac{N}{N+1} - 1\right) \times \frac{\delta}{d_1} + 1\right) \times V_{max} \times d_1 \quad (10)$$

assuming a power law velocity profile, where q is the discharge per unit width: q = Q/B, B is the channel width, N is derived from the best fit of power law, δ is the boundary layer thickness and d_1 is the initial flow water depth. Eq. (10) compared well to the measured specific discharge within 10% for all flow conditions. The results indicated that the free-stream velocity of the experimental data satisfied the continuity principle.

2.4. Unsteady flow experimental conditions

The positive surge was generated by rapidly closing the downstream Tainter gate and the surge propagated upstream. The gate closure time was less than 0.2 s, short enough to have no effect on the surge propagation. For each experiment, all instruments were started 60 s prior to the gate closure, and the sampling ended when the surge front reached the upstream intake structure, to prevent any surge reflection effect.

The ensemble-averaged measurements were performed systematically at x = 8.5 m under controlled flow conditions. The channel slope S_o, Tainter gate opening h after the rapid closure, and opening of the downstream radial gate were adjusted to achieve a relatively wide range of Froude numbers (Table 1). Both breaking and undular surges were experimented. The experimental flow conditions were summarised in Table 1. Further details on the experiments and experimental procedure were reported in Leng and Chanson [19].

3. Flow observations and velocity results

3.1. Presentation

Free-surface observations were conducted for a range of flow conditions encompassing both breaking and undular surge flow conditions. For $Fr_1 < 1.3$, the bore free-surface was smooth and the first wave crest was followed by a train of secondary undulations. For larger Froude numbers ($Fr_1 > 1.3$), a marked roller was observed associated with large scale turbulence and air bubble entrainment (Fig. 2A).

The velocity properties were recorded in both undular and breaking surges (Table 1). The instantaneous longitudinal velocity data showed a rapid deceleration when the water depth increased during the surge passage, for all elevations and Froude numbers (Fig. 4). Fig. 4 presents some instantaneous data for a breaking surge. With undular bores, the longitudinal velocity oscillated out of phase with the oscillations of the free-surface following the bore passage, as previously reported [16]. At low vertical elevations, some recirculation velocity was observed, associated with negative longitudinal velocity components at the end of the deceleration phase, with both undular and breaking surges. For undular surges, the recirculation velocity was seen for $0 < z/d_1 < 0.2$, while some recirculation was observed for $0 < z/d_1 < 0.3$–0.5 with breaking bores. The findings were consistent with past laboratory and numerical experiments for similar Froude numbers [13,17,28], as well as field measurements in prototype breaking bores [8]. The instantaneous transverse and vertical velocity components showed large fluctuations associated with the propagation of tidal bores at all elevations for all Froude numbers. The vertical velocity components initially increased with the early free-surface rise, then decreased before the free-surface reached its maximum value before fluctuating around a zero mean value, the phenomenon being more clearly observed at higher vertical elevations. In undular bores, the vertical velocity component oscillated in phase with the oscillation of the free-surface after the passage of the bore.

3.2. Ensemble-averaged velocity results

The ensemble-averaged velocity and velocity fluctuations highlighted both the rapid longitudinal deceleration and large fluctua-

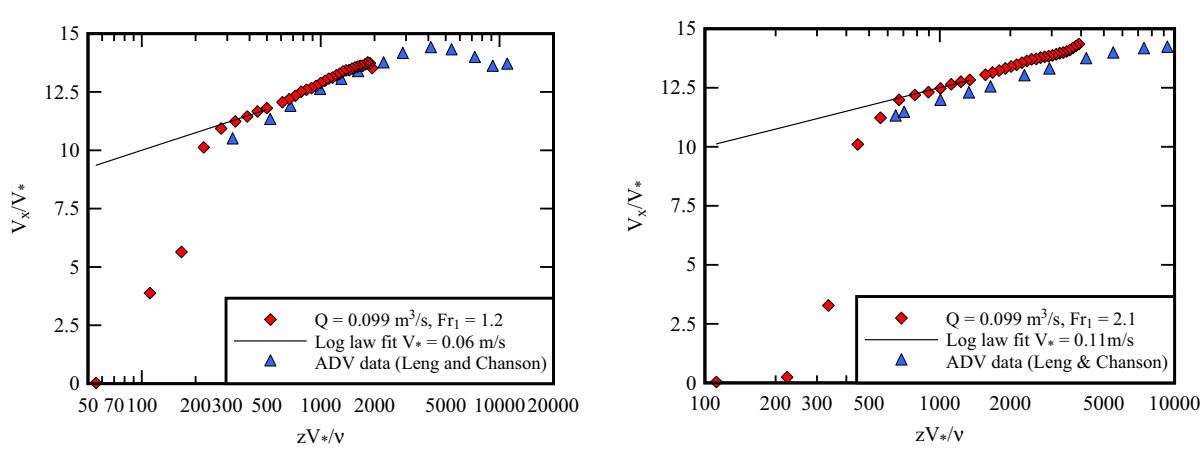

(A) Q = 0.099 m³/s, d_1 = 0.197 m, V* = 0.06 m/s (B) Q = 0.099 m³/s, d_1 = 0.097 m, V* = 0.10 m/s

Fig. 3. Logarithmic velocity profiles in the initially-steady flow at x = 8.5 m - Present Profiler data in red symbols, ADV data [19] in blue symbols and theoretical logarithmic law (Eq. (7)) with a solid black line.

Table 1
Experimental flow conditions for ensemble-averaged Profiler measurements.

S_o	Q (m^3/s)	d_1 (m)	Radial gate opening (m)	h (m)	z_{max}/d_1	Bore type	Instrumentation	U (m/s)	Fr_1
0	0.099	0.169	N/A	0	0.2	Breaking	Profiler & ADMs	1.2	1.6
0	0.103	0.173	N/A	0	0.3	Breaking	Profiler & ADMs	1.3	1.6
0	0.099	0.17	N/A	0	0.7	Breaking	Profiler & ADMs	1.1	1.6
0	0.099	0.196	0.125	0.071	0.2	Undular	Profiler & ADMs	1.0	1.2
0	0.099	0.197	0.125	0.071	0.3	Undular	Profiler & ADMs	1.0	1.2
0	0.099	0.199	0.125	0.071	0.6	Undular	Profiler & ADMs	1.0	1.2
0.0075	0.099	0.097	N/A	0	0.4	Breaking	Profiler & ADMs	0.6	2.1

Notes: d_1: initial flow depth at x = 8.5 m; h: Tainter gate opening after rapid closure; Q: water discharge; S_o: bed slope; z_{max}: vertical elevation of highest point in velocity profile measured above the channel bed; ADM: acoustic displacement meter.

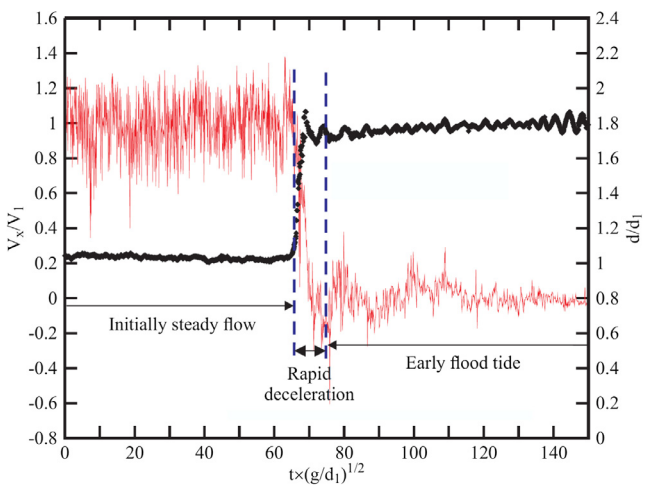

Fig. 4. Time-variation of instantaneous longitudinal velocity V_x and water depth d - Flow conditions: Q = 0.099 m^3/s, Fr_1 = 1.6, z = 0.050 m - Definition sketch highlights different flow phases used for the turbulent integral scale analysis, with 6000 data included in the initially steady flow, between 50 to 200 data in the rapid deceleration phase (rapidly-varied flow), and 1000 data included in the early flood tide phase (unsteady flow).

tions in all velocity components at all elevations for both breaking and undular bores, except for the vertical elevations that were very close to the bed ($z/d_1 < 0.03$). Next to the bed, negative longitudinal velocities were observed at the end of the deceleration phase, indicating a transient flow reversal, under both breaking and undular bores. The finding was similar to earlier results [17,3]. For undular bores, the longitudinal velocity after the bore front passage varied with time in a quasi-periodic manner, with periods of oscillation equal to the free-surface oscillation but out of phase by π. Fig. 5 presents typical time-variations of ensemble-averaged velocity and velocity fluctuations at different vertical elevations for a breaking surge. Herein the instantaneous fluctuations are characterised by the difference between the third and first quartiles (V_{75}–V_{25}) of the data ensemble. For a Gaussian distribution of the data about the mean, (V_{75}–V_{25}) would be equal to 1.3 times the standard deviation [30].

The transverse velocity component in breaking surges was zero on the channel centreline in the initially steady flow. With the passage of the surge, the data showed large fluctuations at all vertical elevations. At vertical elevations slightly below the initial free-surface elevation, the transverse velocity decreased to negative values when the free-surface elevation increased with the bore arrival, indicating a transverse recirculation motion towards the left sidewall, before shifting to negative values, and later fluctuating about zero. In undular bores, the transverse velocity components fluctuated with the free-surface oscillations in a quasi-periodic manner, with periods out of phase by π. With breaking

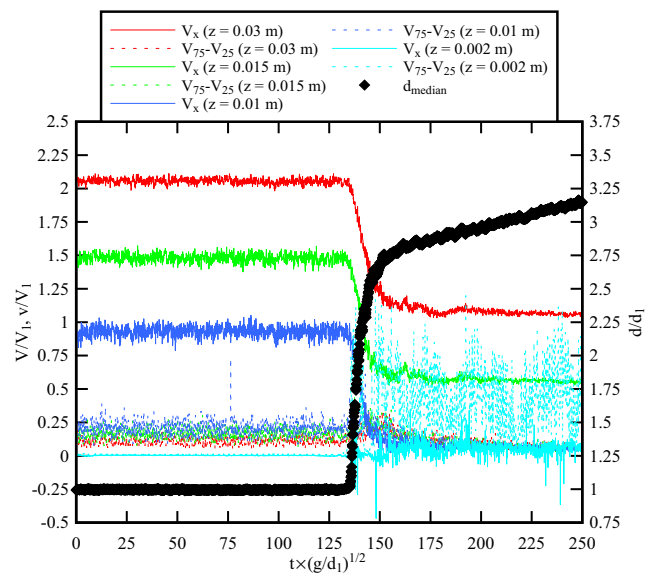

(A) Longitudinal velocity V_x

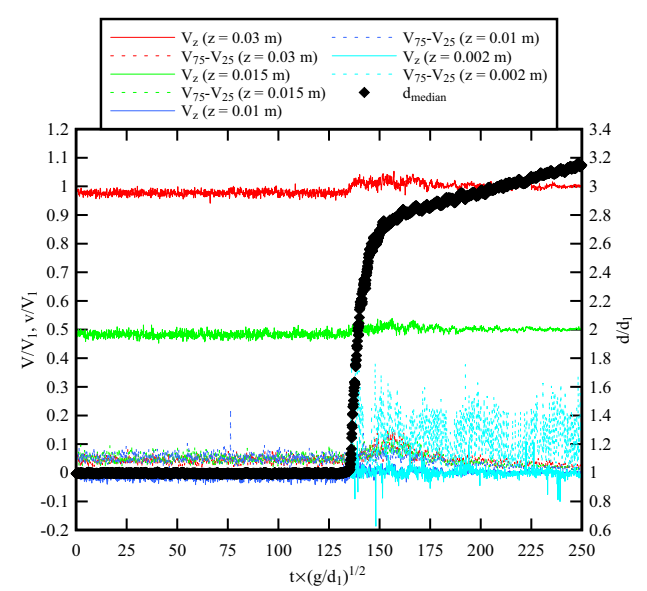

(B) Vertical velocity V_z

Fig. 5. Dimensionless time variations of ensemble-averaged velocity and velocity fluctuations in the longitudinal (A) and vertical (B) directions for a velocity profile from z = 0.001 m to 0.035 m with ensemble-averaged water depth measured at the velocity sampling location - Flow conditions: Q = 0.099 m^3/s, Fr_1 = 2.1 - Velocity offset by +0.5 for two higher elevations.

surges, the vertical velocity component at vertical elevations close to the free-surface showed an initial increase to positive values

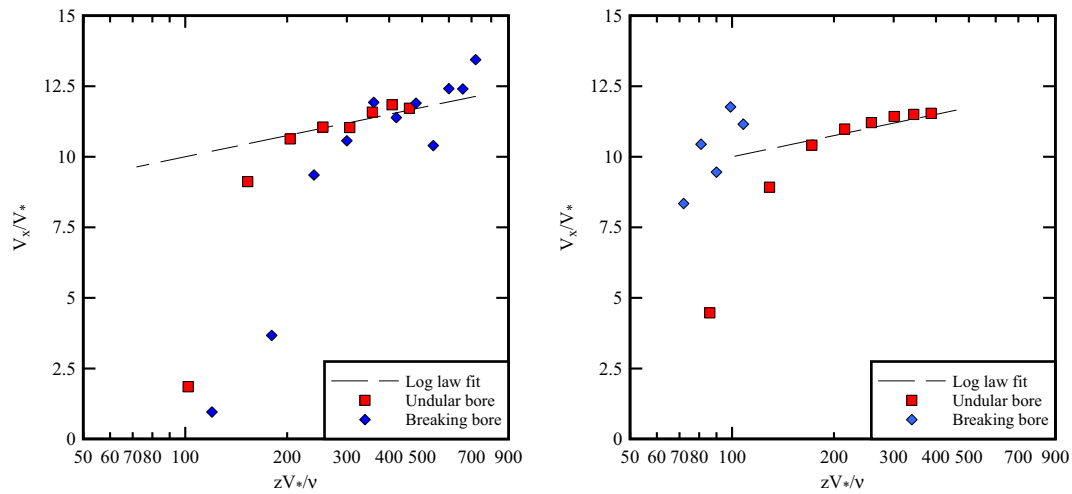

(A, Left) Rapid deceleration phase (B, Right) Early flood tide phase

Fig. 6. Comparison of ensemble-averaged median longitudinal velocity with the logarithmic profile (law of the wall) during the rapid deceleration and early flood tide phases for propagating breaking and undular surges - Flow conditions: Q = 0.099 m^3/s, d_1 = 0.097 m, Fr_1 = 2.1, Breaking bore & Q = 0.099 m^3/s, d_1 = 0.197 m, Fr_1 = 1.2, Undular bore.

with the early rise in free-surface, followed by a decrease before the free-surface reached its maximum. Behind the surge front, the vertical velocity oscillated in a quasi-periodic manner linked to the oscillation of free-surface. The periods of the vertical velocity oscillations seemed to be equal to and out of phase by $\pi/2$ compared to observed free-surface oscillations.

The instantaneous velocity fluctuations in the longitudinal, transverse and vertical directions showed an abrupt increase associated with the passage of positive surge at all vertical elevations for all Froude numbers. The magnitudes of velocity fluctuations were the largest at elevations close to the bed. The longitudinal velocity data were typically associated with the largest instantaneous velocity fluctuations, compared to the transverse and vertical components. The maximum velocity fluctuations occurred with some time lag Δt_V after the onset of free-surface rise, as previously observed [19]. The maximum velocity fluctuation $(V_{75}-V_{25})_{max}$ was defined as the first marked peak in terms of $(V_{75}-V_{25})$ after the surge arrival. Both the maximum velocity fluctuations $(V_{75}-V_{25})_{max}$ and associated time lag Δt_V were quantified for the present data.

The vertical profiles of the median longitudinal velocity within the wall region: i.e., $\rho \times V_* \times z/\mu > 70$ and $z/\delta < 0.2$, were tested during the rapid deceleration phase and the early flood tide phase. Herein the early flood tide phase is defined as the phase starting immediately after the end of the rapid deceleration phase (Fig. 3). Typical data are plotted in Fig. 6 where the data are compared to the log law, for undular and breaking bores (Fr_1 = 1.2 and 2.1 respectively). Fig. 6A presents results for the deceleration phase while Fig. 6B shows early flood tide data immediately after the rapid deceleration. Altogether the data demonstrated that, during the rapid deceleration phase, the majority of the data within the wall region compared well to the log law, although a larger scatter was observed during the breaking bores. During the early flood tide phase, the longitudinal velocity profile for a breaking bore with Fr_1 = 2.1 did not as agree as well with the log law. The shear velocity V_* obtained from the best fit of log law differed between the two phases: that is, $V_* \approx 0.060$ m/s for the rapid deceleration and $V_* \approx 0.009$ m/s during the early flood tide. Both values were lower than the steady flow shear velocity: V_* = 0.110 m/s. For undular bores, the data during both the rapid deceleration and early flood tide phases were close qualitatively and quantitatively. The best fit of the log law yielded: V_* = 0.050 m/s, a result close to the steady flow shear velocity (V_* = 0.060 m/s).

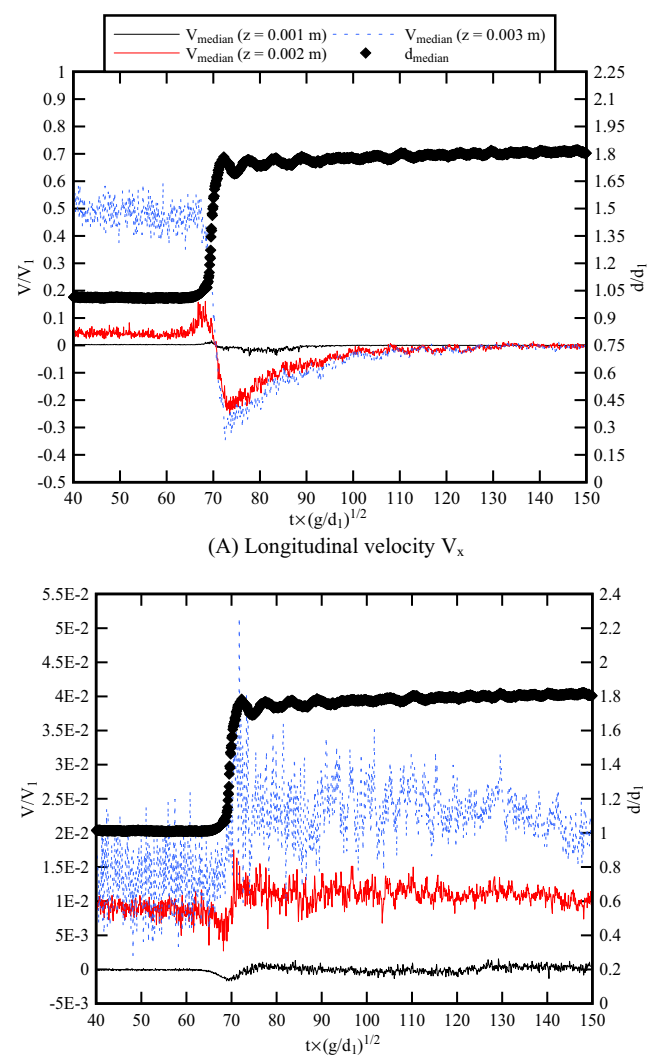

(A) Longitudinal velocity V_x

(B) Vertical velocity V_z

Fig. 7. Ensemble-averaged time-variations of longitudinal and vertical velocity components and free-surface elevation at close vicinity of the channel bed - Transverse and vertical velocity offset by +0.01 for the two higher elevations - Flow conditions: Q = 0.099 m^3/s, Fr_1 = 1.6, S_o = 0.

In the very close vicinity of the bed ($z/d_1 < 0.01–0.02$), the ensemble-averaged longitudinal velocity data showed first some acceleration with the initial free-surface rise prior to the arrival of the roller, a phenomena associated with breaking bores of $Fr_1 < 2$ (Fig. 7A). For bores with $Fr_1 > 2$, a slight initial longitudinal acceleration was also observed close to bed, however not as significant as bores with lower Froude numbers. This very-short period of initial longitudinal acceleration lasted only for a dimensionless time of less than 3–5, corresponding in real time to less than 0.6 s, before the rapid deceleration phase, during rapid free-surface rise when the bore front passed (Fig. 7A). This initial longitudinal acceleration was more clearly marked at the second lowest vertical elevation in the velocity profile (z = 0.002 m) compared to at the lowest vertical elevation (z = 0.001 m). Simultaneously, the vertical velocity decreased to negative valued, to maintain conservation of mass and momentum at the locations where an initial longitudinal acceleration was observed (Fig. 7). The transverse velocity showed some large fluctuation, although no obvious pattern in time-variations was observed. At vertical elevations above z = 0.003 m ($z/d_1 > 0.01–0.02$), the initial longitudinal acceleration phase disappeared, and the longitudinal velocity data showed an immediate deceleration shortly after the onset of free-surface rise. This was accompanied by marked positive vertical velocity components, consistent with previous data.

The initial longitudinal acceleration in the bed vicinity was observed in breaking bores as well as in undular bores. Previous numerical models reported small transient vortical structures formed under the gradual free-surface rise immediately before the roller toe in breaking bores, and under the point where the free-surface turned to rise in undular bores [28,14]. The observed longitudinal acceleration and vertical deceleration were believed to be associated with the presence of these vortical structures.

4. Reynolds stresses and integral turbulent scales

4.1. Turbulent Reynolds stresses

The ensemble-averaged Reynolds stress data highlighted large shear stress magnitudes and large shear stress fluctuations at all elevations associated with the bore passage, for all flow conditions. The time-variations of the ensemble-median Reynolds stress components and corresponding shear stress fluctuations were comparable to previous results, albeit obtained with a different

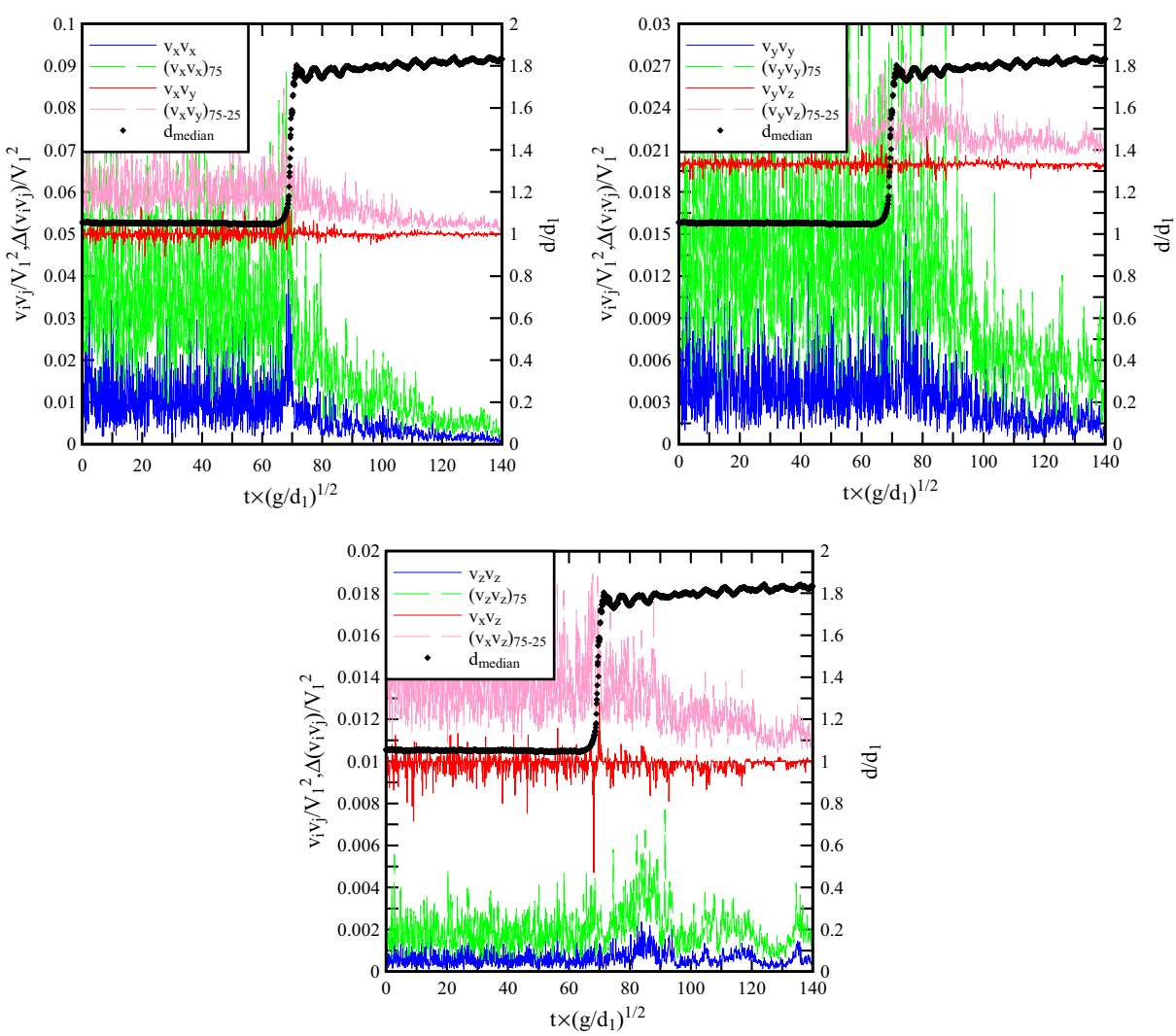

Fig. 8. Ensemble-averaged time-variations of Reynolds stress components at vertical elevation z = 0.05 m in a velocity profiler from z = 0.015 m to 0.05 m - Flow conditions: $Q = 0.103\ m^3/s$, $Fr_1 = 1.6$ - Tangential stresses offset by +0.05, +0.02 and +0.01 for components $v_x \times v_y$, $v_y \times v_z$ and $v_x \times v_z$, respectively.

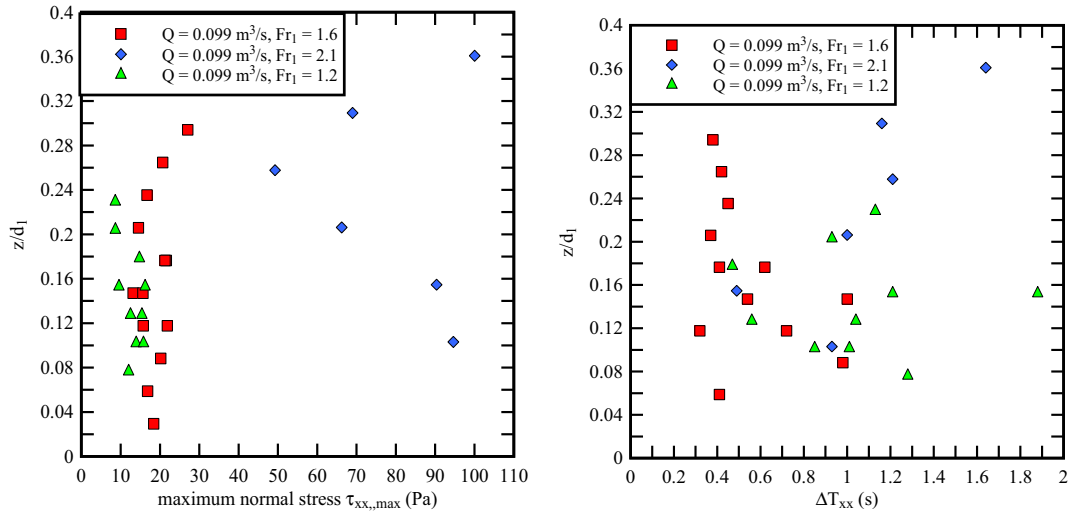

Fig. 9. Vertical profile of maximum ensemble-median normal Reynolds stress $\tau_{xx,max}$ during a positive surge passage and associated time lag ΔT_{xx}.

instrumentation [3,6,15]. Fig. 8 presents typical ensemble-averaged Reynolds stresses and associated fluctuations for a breaking surge. Herein the normal stress fluctuations are characterised by the third quartile $(v_i \times v_i)_{75}$, while the tangential stress fluctuations are presented in terms of the difference between the third and first quartiles. For the range of investigated flow conditions (Table 1), all Reynolds stress components showed a marked increase in magnitudes and in fluctuations at all vertical elevations during and following the bore passage (see below). Maximum stress magnitudes were reached typically at the same time as the maximum stress fluctuations were observed: that is, shortly after the arrival of the bore front.

The measurements highlighted maximum Reynolds stresses and stress fluctuations occurring shortly after the arrival of the surge front, for all Reynolds stress components at all vertical elevations throughout the initial water column ($0 < z/d_1 < 1$), for Froude numbers ranging from 1.2 to 2.2. The time lag ΔT between the arrival time of the bore front and the occurrence of the maximum shear stress magnitudes (or shear stress fluctuations) were documented [19]. Overall, breaking bores with higher Froude numbers were associated with larger maximum Reynolds stresses and shear stress fluctuations at similar dimensionless elevations, compared to undular bores and breaking bores with lower Froude numbers. For bores with the same Froude number, larger maximum shear stresses and shear stress fluctuations were observed at higher vertical elevations, possibly linked to the large scale vortical structures generated in the wake of the bore front, next to the free-surface. The normal stress components were typically associated with more pronounced peaks in terms of median shear stress and shear stress fluctuations, compared to the tangential stress components. The tangential stress component $v_x \times v_z$ showed negative maxima irrelevant of the Froude numbers. In terms of time lag, ΔT and Δt_V respectively, the maximum shear stress magnitudes and the maximum stress fluctuations occurred simultaneously, within ±0.1 s.

Focusing on the ensemble-averaged normal Reynolds stress component τ_{xx}, the data presented a most distinctive maximum $(\tau_{xx})_{max}$ during the positive surge passage (Fig. 8 Top Left). The vertical distributions of maximum ensemble-median stresses $\tau_{xx,max}$ and associated time lags ΔT_{xx} are shown in Fig. 9 in a dimensional form for all flow conditions. Overall, the data highlighted high median stress levels, ranging from 10 to 110 Pa, throughout the lower water column (Fig. 9). The maximum median stresses during the breaking bore with the highest Froude number were in general much larger than those of bores with smaller Froude numbers at all vertical elevations. For lower Froude numbers (Fr_1 = 1.2 and 1.6), the maximum stress levels were close, fluctuating between 10 to 30 Pa for all vertical elevations. For the highest Froude number (Fr_1 = 2.1), the variation in maximum stresses with vertical elevation was large. The results showed that some large median shear stress range could occur up to 50 Pa to 110 Pa within the boundary layer. Similarly, for all bore flow conditions, the vertical profile of the time lag showed some large range, from 0.2 s to 2 s, with data scatter of up to 1 s within the water clumn. Despite some scatter, the vertical distribution of maximum Reynolds stresses provided information on the range and magnitude of shear stress levels in the unsteady rapidly-varied flow motion.

4.1.1. Discussion

The instantaneous Reynolds stress data were analysed in terms of the probability density functions (PDFs) of normal and tangen-

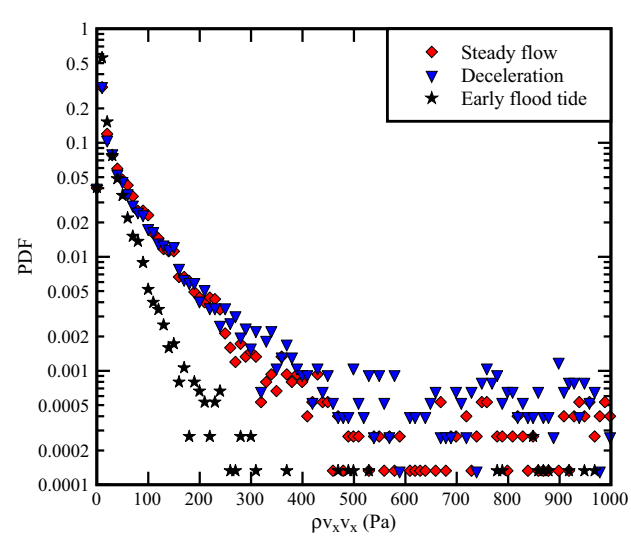

Fig. 10. Probability density functions of normal Reynolds stresses $\rho \times v_x \times v_x$ before, during and after a breaking bore passage - Flow conditions: Q = 0.099 m³/s, Fr_1 = 2.1, z/d_1 = 0.1 - Vertical axes in logarithmic scale.

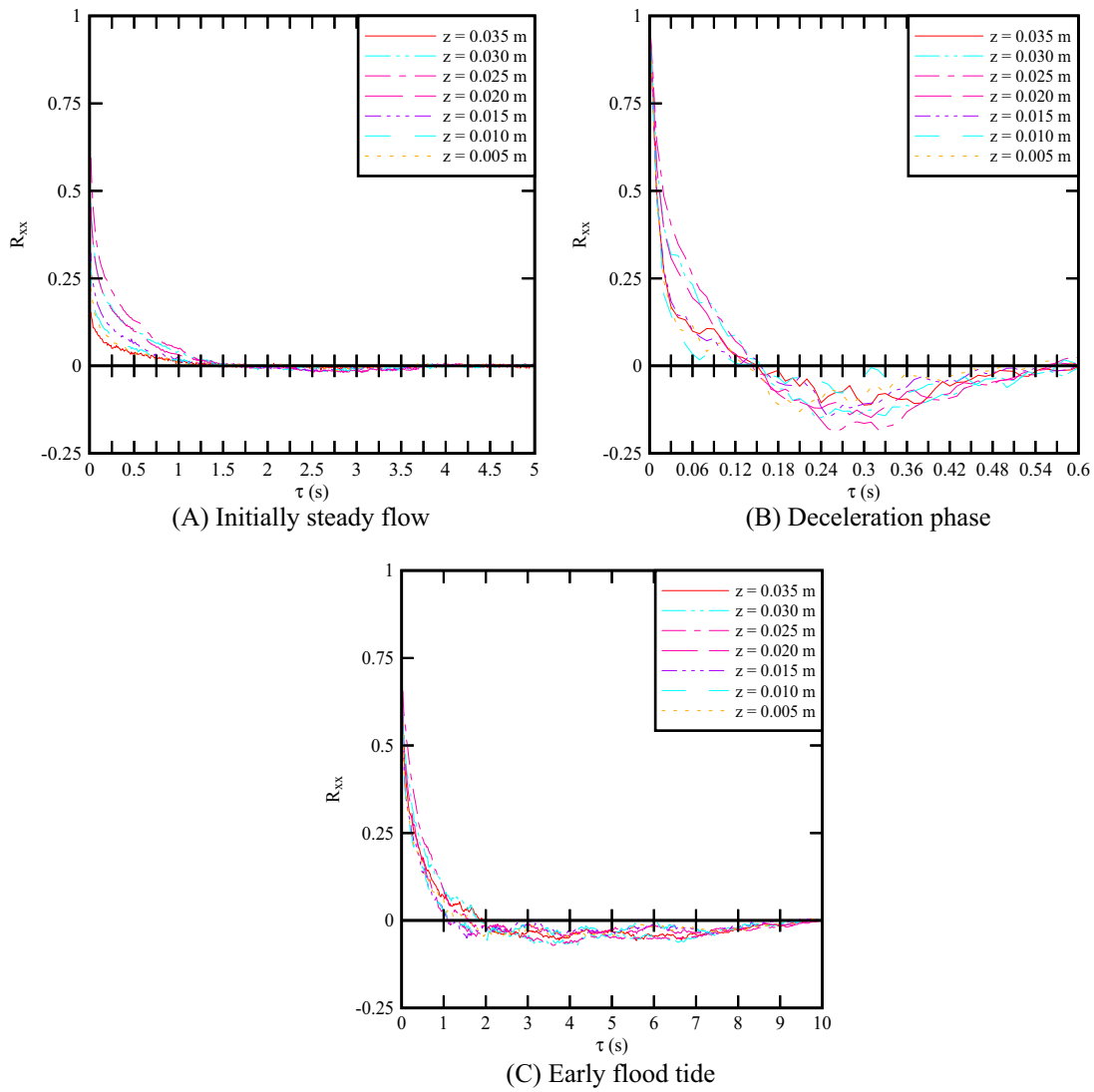

Fig. 11. Typical auto-correlation functions of the longitudinal velocity over different phases - Flow conditions: Q = 0.099 m_3/s, Fr_1 = 1.6, z/d_1 = 0–0.207.

tial stresses over a short time period (within 3 s) before, during and after the bore passage. Fig. 10 illustrates a typical result for the normal stress component $\rho \times v_x \times v_x$. Overall, the results showed comparable trends before, during and after the surge passage: e.g., for $\rho \times v_x \times v_x$, instantaneous levels up to 100–200 Pa, although very few larger stress occurrences were recorded (Fig. 10). The data demonstrated marked peaks associated with very similar stress levels (~10–50 Pa) before, during and after the surge passage, albeit a lesser amount of very large shear stresses (>200 Pa) were recorded during the early flood tide after the rapid flow deceleration.

4.2. Turbulent integral scales

The auto-correlation functions of all velocity components were calculated at each sampling point for three flow phases: (a) the initially steady flow before surge arrival, (b) the rapidly-varied flow region during the surge passage or deceleration phase, and (c) the unsteady flow region after the front passage or early flood tide (Fig. 4). Fig. 11 shows typical auto-correlation functions R_{xx} of the longitudinal velocity component measured at different vertical elevations z for each flow phase. Note the different horizontal sales

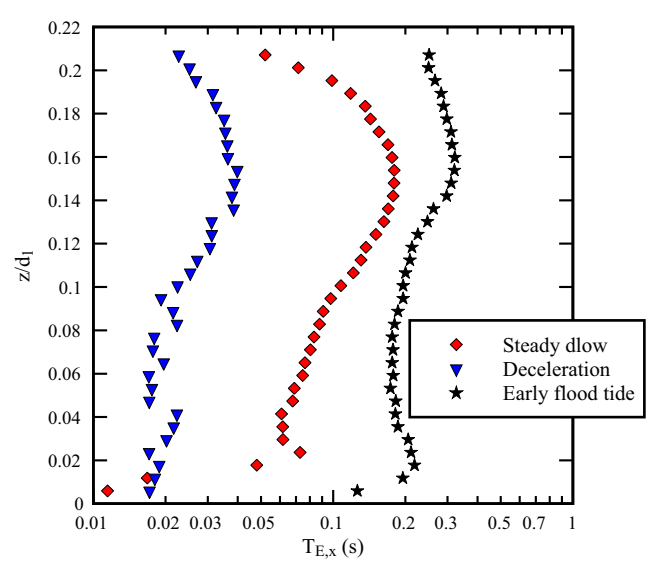

Fig. 12. Eulerian auto-correlation time scale of the longitudinal velocity component for the three flow phases - Flow conditions: Q = 0.099 m^3/s, Fr_1 = 1.6, z/d_1 = 0.006–0.207.

between graphs. For all velocity components and flow conditions, the auto-correlation functions exhibited a bell shape, regardless of the flow phase and elevation. The early flood tide phase was associated with the longest period of positive auto-correlation, while the rapid deceleration phase was characterised by relatively large negative correlations for a time lag τ greater than 0.1 s.

The Eulerian integral time scale T_E was deduced from the integration of auto-correlation functions. Fig. 12 presents typical vertical profiles of Eulerian integral time scale for the longitudinal velocity direction during the three flow phases. While the shape might not be truly meaningful, the data provided some order of magnitude and range of auto-correlation time scales. For all velocity components and flow conditions, the Eulerian time scales ranged from 10^{-2} s to 3×10^{-1} s, corresponding to a dimensionless range of $T_E \times (g/d_1)^{1/2}$ between 10^{-2} and 3. In the initially steady flow, the Eulerian time scales were comparable to previous laboratory studies [29,8]. The present results are reported in Appendix A.

For all velocity components, the auto-correlation time scales were consistently larger after the positive surge, during the early flood tide, inclusive of the deceleration phase and early flood tide in the present study. The present results were consistent with a couple of field studies (Appendix A). The data further showed no clear trend in terms of relative vertical elevation and Froude number. The auto-correlation time scales in the longitudinal velocity direction were generally larger than those of the other velocity components, with $T_{E,y}/T_{E,x} \sim 0.3$–0.8 and $T_{E,z}/T_{E,x} \sim 0.7$–1.5. The finding implied that the turbulence was anisotropic, in agreement with previous laboratory and field studies.

4.2.1. Integral turbulent time and length scales

The turbulent integral time and length scales in the vertical flow direction were derived from the ensemble-averaged cross-correlation functions, and the results are presented in terms of three main flow phases: (a) initially steady flow, (b) rapid deceler-

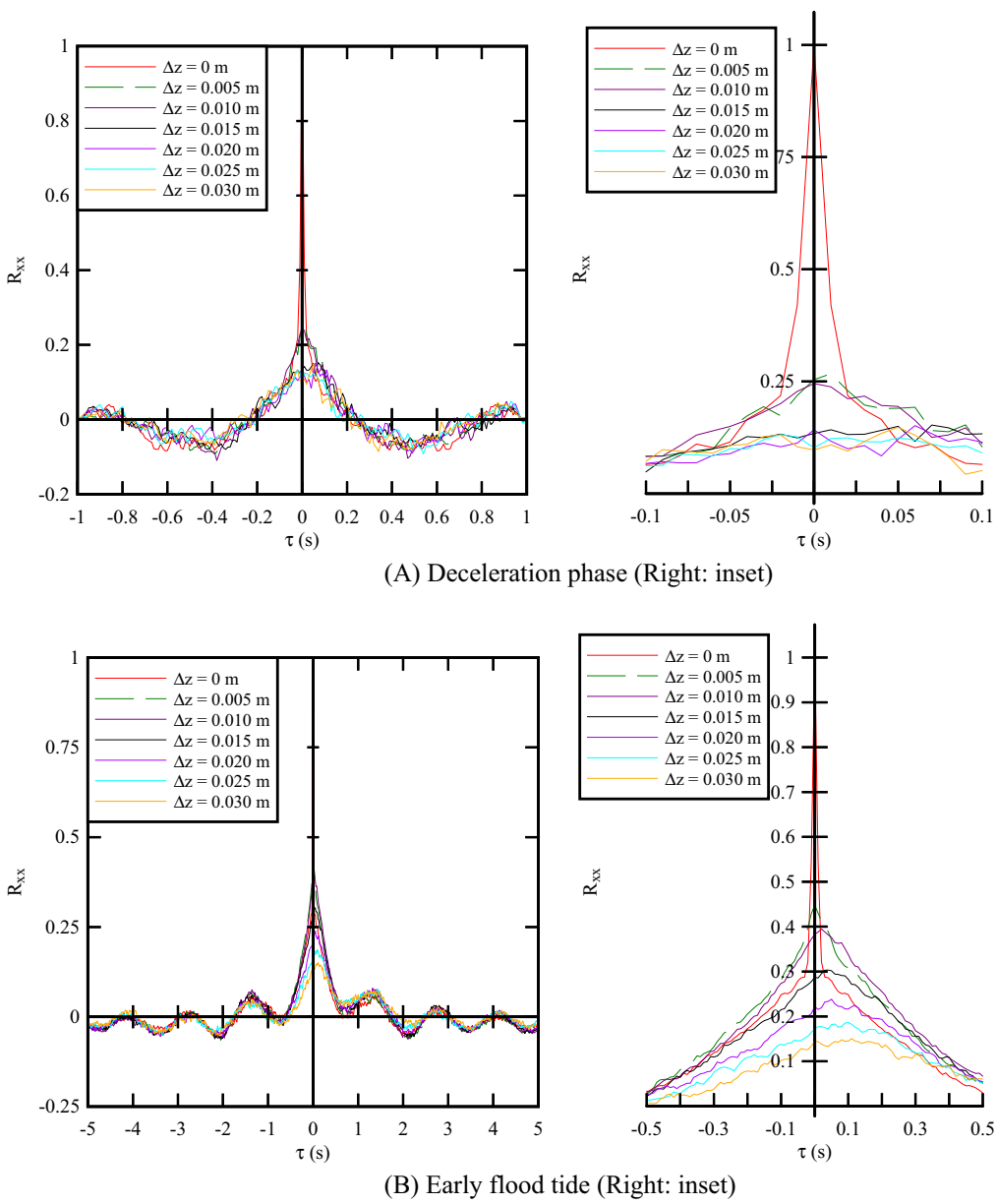

Fig. 13. Ensemble-averaged cross-correlation functions of the longitudinal velocity component for the rapid deceleration phase and the early flood tide after surge passage - Flow conditions: Q = 0.099 m^3/s, Fr_1 = 1.

ation phase, and (c) early flood tide immediately after surge passage. Fig. 4 shows the definition of the three phases. For the initially steady flow, the analysis was performed for the first 60 s of the data sets. The rapid deceleration phase was taken from the start of the free-surface rise, corresponding to the first instance when the first derivative of the water depth became non-zero, to the instance of the minimum streamwise velocity reached at the end of the longitudinal deceleration. All velocity data were analysed within this duration typically ranging from 0.5 s to 2 s. The analysis in the early flood tide was performed for 10 s, immediately following the end of the deceleration phase. The methodology was applied consistently to all flow conditions.

The ensemble-averaged correlation functions in the steady flow region for all flow conditions exhibited similar shapes and orders of magnitudes as those analysed using the instantaneous velocity data, although the absolute values of maximum cross-correlations were typically lower than those derived from instantaneous fluctuation data. Typical ensemble-averaged cross-correlation functions of the longitudinal velocity during the rapidly-varied and unsteady flow regions for bores of two Froude numbers are presented respectively in Fig. 13A and B. The results highlighted differences in terms of shapes of the cross-correlation functions. During the deceleration phase (Fig. 13A), all cross-correlation functions showed a quasi-symmetrical shape, with two local minima on each side of the marked maximum. The absolute values of the local minima were less than that of the maximum for all Froude numbers and elevations. The absolute maximum correlation occurred at positive time lags during the initially steady and deceleration phases, and these time lags increased with increasing distance from the reference point (Fig. 13A, Inset). The trend suggested the formation of and occurrence of large vortical structures at higher vertical elevations. During the early flood tide, however, the time lags became negative for breaking bores ($Fr_1 = 1.6$), indicating that large vortical structures were formed next to the channel bed and advected upwards. For breaking bores with higher Froude number ($Fr_1 = 2.1$), the time lags were almost zero, hinting that large vortical structures, possibly exceeding the length of the profile, were formed and detected almost simultaneously by all sampling points along a profile. In undular bore ($Fr_1 = 1.2$), the cross-correlation functions during the early flood tide showed a quasi-symmetrical shape, with periodic variations for the positive and negative time lags (Fig. 13B). The time lags corresponding to the maximum cross-correlations for undular bore were positive throughout the three flow phases.

The turbulent integral time and length scales are summarised in a tabular form in Appendix B for the longitudinal, transverse and vertical velocity components for all flow conditions during different flow phases. The results are compared to a previous laboratory study [29]. Overall the data highlighted that the propagation of positive surge in an open channel was an anisotropic process, with the turbulent time and length scales being much larger with the longitudinal and vertical velocity components, than in the transverse component. That is, the present data implied $L_{z,y}/L_{z,x} \sim 0.1–0.9$ and $T_{z,y}/T_{z,x} \sim 0.1–0.6$ (Appendix B). A majority of turbulent time and length scales in the vertical velocity direction were larger than those in the longitudinal velocity direction, with $L_{z,z}/L_{z,x} \sim 1.1–7.3$ and $T_{z,z}/T_{z,x} \sim 1.1–14.4$, for all the flow conditions. Physically, the data would suggest that the vertical size and lifespan of vortical structures were larger in the vertical direction compared to those in the horizontal directions. Visual observations in breaking bores highlighted indeed large helicoidal bubbly structures, elongated mostly along the vertical direction, which occurred both in the roller and the bubbly flow regions immediately behind the roller (Fig. 14). The experimental results could be representations of such vortical structures. Note however that earlier observations of neutrally-buoyant particle trajectories suggested flatter structures in undular surges [7].

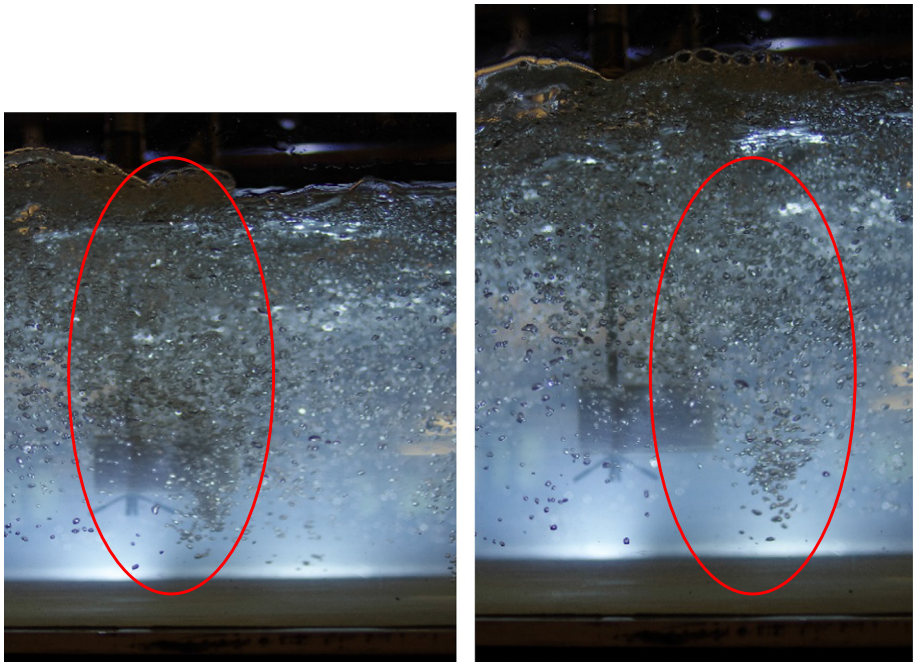

Fig. 14. Photographs of vertical vortices formed in the bubbly flow region following the breaking surge roller - Flow conditions: $Q = 0.099\ m^3/s$, $Fr_1 = 2.1$, surge propagation from right to left.

Immediately after the surge passage, the early flood tide phase was associated with large turbulent time and length scales, compared to the initially steady flow and deceleration phases. The integral turbulent time scales were an order of magnitude larger than those during the steady flow and rapid deceleration phases in the lower water column, regardless of velocity components and initial flow conditions, albeit the Integral turbulent time and length scales seemed to decrease with increasing vertical elevations.

The present study may be compared with a past laboratory data [29] (Appendix B). In terms of quantitative results, both the turbulent integral time and length scales were of the order of magnitude, albeit larger herein. Possibly because the present experiments were performed in a much larger facility with higher Reynolds numbers. Note that previous data were collected by point measurements using two ADVs, separated at 6 transverse separation intervals, with 5 experiments repeated for each separation [29]. Herein the study was performed in the vertical direction by sampling simultaneous 35 points, each two adjacent points separated at 1 mm, and repeated 25 times. The present spatial resolution was much finer, and the correlations between velocity signals were expected to be higher, as all points were sampled at the same time.

5. Conclusion

Unsteady velocity profiling measurements were conducted in positive surges at relatively high frequency (100 Hz). Both undular and breaking surges were investigated with Froude numbers ranging from 1.2 to 2.1. An ensemble-averaged measurement technique was used: all experiments were repeated 25 times.

The profiling data indicated that the longitudinal velocity profile within the inner region of the turbulent boundary layer followed the log law before, during and after the surge passage. The Eulerian time scale, turbulent time and length scale results indicated that the propagation of positive surge in an open channel flow was an anisotropic process, with larger time and length scales in the longitudinal and vertical directions. The integral turbulent time and length scales were of an order of magnitude between 1 ms and 100 ms, and 10^{-3} m and 10^{-1} m respectively, similar to previous laboratory and field data. The present results indicated that the propagation of a positive surge generated an unsteady and anisotropic turbulence. Dimensionless turbulent time and length scale data yielded $L_{z,z}/L_{z,x} \sim 1.1–7.3$ and $T_{z,z}/T_{z,x} \sim 1.1–14.4$ for all the flow conditions, suggesting vortical structures with longer dimensions in the vertical direction compared to those in the horizontal directions.

Overall, the results demonstrated that the propagation of positive surges is a highly unsteady turbulent process. Unsteady velocity profiling provided further types of data for CFD validation. While present results compared well with existing CFD outcomes, they will expand the typology of computational validation based upon physical data.

Acknowledgments

The authors thank Dr. Hang Wang (The University of Queensland, Australia) and Mr. Gangfu Zhang (The University of Queensland, Australia) for their respective involvement, and Dr. Bruce Macvicar (University of Waterloo, Canada) and Dr. Heide Friedrich (University of Auckland, New Zealand) for helpful comments. They acknowledge the technical assistance of Jason Van Der Gevel and Stewart Matthews (The University of Queensland). The financial support through the Australian Research Council (Grant DP120100481) is acknowledged.

Appendix A

Auto-correlation time scales in tidal bores - comparison between laboratory and field data.

Reference	Site	Instrument	Sampl. rate Hz	Fr_1	d_1[a] m	z/d_1	$T_{E,y}$/ Steady flow	$T_{E,x}$ Rapid deceleration	$T_{E,z}$/ Early flood tide	$T_{E,z}$/ Steady flow	$T_{E,x}$ Rapid deceleration	Ratio to Early flood tide	Ratio to T_{Ex}	Ratio to T_{Ey}	Ratio to T_{Ez}	Remark
Reungoat et al. [25]	Garonne River	Sontek microADV	50	1.02	2.91	0.646	–	–	–	–	–	–	21.7	–	–	Field data
Reungoat et al. [26]	Garonne River	Nortek Vectrino+	200	1.27	2.05	0.522	0.39	–	0.46	0.39	–	0.09	9.7	11.3	2.33	Field data
Present study	Laboratory	Nortek VectrinoB	100	1.6	0.17	0.006–0.73	0.36	0.65	0.81	0.83	1.14	1.10	7.1	16.1	11.2	Average values
		Profiler		1.2	0.199	0.005–0.63	0.32	0.71	0.34	1.11	1.49	0.67	1.68	2.28	1.88	
				2.1	0.097	0.01–0.36	–[b]	–[b]	–	1.45	0.91	0.75	9.4	–[b]	10.1	

[a] Water depth at ADV.
[b] For $Fr_1 = 2.1$, there was no V_y data, because the receivers for V_y component were affected by in the wake behind the receivers: and all velocity characteristics in the y-direction under this flow configuration were deemed erroneous and not considered.

Appendix B

Unsteady turbulent integral time and length scales for all velocity components and flow conditions.

Present study					Steady		Deceleration		Early flood tide		Steady		Deceleration		Early flood tide		Steady		Deceleration		Early flood tide	
	Q (m^3/s)	Fr_1	d_1 (m)	z_{max}/d_1	$L_{z,x}$ (m)	$T_{z,x}$ (s)	$L_{z,x}$ (m)	$T_{z,x}$ (s)	$L_{z,x}$ (m)	$T_{z,x}$ (s)	$L_{z,y}$ (m)	$T_{z,y}$ (s)	$L_{z,y}$ (m)	$T_{z,y}$ (s)	$L_{z,y}$ (m)	$T_{z,y}$ (s)	$L_{z,z}$ (m)	$T_{z,z}$ (s)	$L_{z,z}$ (m)	$T_{z,z}$ (s)	$L_{z,z}$ (m)	$T_{z,z}$ (s)
	0.099	1.6	0.169	0.207	0.007	0.073	0.009	0.040	0.010	0.210	0.004	0.011	0.004	0.014	0.009	0.217	0.009	0.021	0.009	0.026	0.015	0.226
	0.099	1.6	0.173	0.289	0.007	0.067	0.010	0.019	0.009	0.207	0.004	0.006	0.005	0.012	0.008	0.142	0.010	0.020	0.008	0.018	0.018	0.343
	0.099	1.6	0.170	0.735	0.003	0.006	0.009	0.010	0.009	0.181	0.003	0.003	0.005	0.005	0.008	0.111	0.013	0.027	0.015	0.019	0.020	0.301
	0.099	1.2	0.196	0.199	0.005	0.062	0.007	0.018	0.010	0.118	0.003	0.007	0.004	0.005	0.005	0.025	0.008	0.018	0.008	0.013	0.012	0.037
	0.099	1.2	0.197	0.254	0.005	0.050	0.006	0.022	0.009	0.080	0.003	0.005	0.003	0.004	0.004	0.016	0.008	0.018	0.008	0.022	0.012	0.036
	0.099	1.2	0.199	0.628	0.002	0.003	0.004	0.005	0.007	0.038	0.003	0.004	0.004	0.005	0.004	0.010	0.016	0.048	0.016	0.032	0.018	0.061
	0.099	2.1	0.097	0.361	0.003	0.010	0.004	0.014	0.006	0.101	–	–	–	–	–	–	0.004	0.005	0.006	0.018	0.013	0.095

Simon and Chanson [29][a]					Early flood tide		Early flood tide	
	Q (m^3/s)	Fr_1	d_1 (m)	z_{max}/d_1	$L_{y,x}$ (m)	$T_{y,x}$ (s)	$L_{y,y}$ (m)	$T_{y,y}$ (s)
	0.053	1.6	0.112	0.110	0.004	0.038	0.007	0.039
				0.270	0.007	0.058	0.010	0.049
				9.450	0.006	0.050	0.010	0.051
				0.630	0.007	0.051	0.009	0.037
	0.053	1.3	0.112	0.110	0.005	0.042	0.006	0.033
				0.270	0.006	0.053	0.010	0.032
				9.450	0.008	0.062	0.010	0.027
				0.630	0.008	0.055	0.012	0.025

[a] ADV point measurements collected at a fixed vertical elevation and over different transverse separations Δy, calculation based upon velocity fluctuations.

References

[1] F. Benet, J.A. Cunge, Analysis of experiments on secondary undulations caused by surge waves in trapezoidal channels, J. Hydraul. Res. 9 (1) (1971) 11–33, IAHR.

[2] H. Chanson, The Hydraulics of Open Channel Flow: An Introduction, second ed., Butterworth-Heinemann, Oxford, UK, 2004, 630 pages.

[3] H. Chanson, Unsteady turbulence in tidal bores: effects of bed roughness, J. Waterway, Port, Coastal, Ocean Eng. 136 (5) (2010) 247–256, http://dx.doi.org/10.1061/(ASCE)WW.1943-5460.0000048, ASCE.

[4] H. Chanson, Momentum considerations in hydraulic jumps and bores, J. Irrigat. Drain. Eng. 138 (4) (2012) 382–385, http://dx.doi.org/10.1061/(ASCE)IR.1943-4774.0000409, ASCE.

[5] H. Chanson, Applied Hydrodynamics: An Introduction, CRC Press, Taylor & Francis Group, Leiden, The Netherlands, 2014, p. 448, 448 pages & 21 video movies (ISBN 978-1-138-00093-3).

[6] H. Chanson, N.J. Docherty, Turbulent velocity measurements in open channel bores, Europ. J. Mech. B/Fluids 32 (2012) 52–58, http://dx.doi.org/10.1016/j.euromechflu.2011.10.001.

[7] H. Chanson, K.K. Tan, Turbulent mixing of particles under tidal bores: an experimental analysis, J. Hydraul. Res. 48 (5) (2010) 641–649, http://dx.doi.org/10.1080/00221686.2010.512779, IAHR.

[8] H. Chanson, Y.H. Toi, Physical modelling of breaking tidal bores: comparison with prototype data, J. Hydraul. Res. 53 (2) (2015) 264–273, http://dx.doi.org/10.1080/00221686.2014.989458, IAHR.

[9] H. Favre, Etude Théorique et Expérimentale des Ondes de Translation dans les Canaux Découverts. ('Theoretical and Experimental Study of Travelling Surges in Open Channels'.) Dunod, Paris, France, 1935 (in French).

[10] D.G. Goring, V.I. Nikora, Despiking acoustic doppler velocimeter data, J. Hyd. Eng. 128 (1) (2002) 117–126, ASCE, Discussion: Vol. 129, No. 6, pp. 484–489..

[11] J.O. Hinze, Turbulence, second ed., McGraw-Hill Publ., New York, USA, 1975.

[12] F.M. Henderson, Open Channel Flow, MacMillan Company, New York, USA, 1966.

[13] H.G. Hornung, C. Willert, S. Turner, The flow field downstream of a hydraulic jump, J. Fluid Mech. 287 (1995) 299–316.

[14] N. Khezri, Modelling Turbulent Mixing and Sediment Process Beneath Tidal Bores: Physical and Numerical Investigations Ph.D. thesis, School of Civil Engineering, The University of Queensland, Brisbane, Australia, 2014, 267 pages.

[15] N. Khezri, H. Chanson, Undular and breaking tidal bores on fixed and movable gravel beds, J. Hydraul. Res. 50 (4) (2012) 353–363, IAHR.

[16] C. Koch, H. Chanson, Turbulent mixing beneath an undular bore front, J. Coastal Res. 24 (4) (2008) 999–1007, http://dx.doi.org/10.2112/06-0688.1.

[17] C. Koch, H. Chanson, Turbulence measurements in positive surges and bores, J. Hydraul. Res. 47 (1) (2009) 29–40, http://dx.doi.org/10.3826/jhr.2009.2954, IAHR.

[18] X. Leng, H. Chanson, Turbulent advances of a breaking bore: preliminary physical experiments, Exp. Thermal Fluid Sci. 62 (2015) 70–77, http://dx.doi.org/10.1016/j.expthermflusci.2014.12.002.

[19] X. Leng, H. Chanson, Unsteady Turbulent Velocity Profiling in Open Channel Flows and Tidal Bores using a Vectrino Profiler Hydraulic Model Report No. CH101/15, School of Civil Engineering, The University of Queensland, Brisbane, Australia, 2016, 118 pages.

[20] J.A. Liggett, Fluid Mechanics, McGraw-Hill, New York, USA, 1994.

[21] I. Nezu, H. Nakagawa, Turbulence in Open-Channel Flows, in: IAHR Monograph, IAHR Fluid Mechanics Section, Balkema Publ., Rotterdam, The Netherlands, 1993, 281 pages.

[22] V. Nikora, Personal Communication on the Suitability of ADV Despiking Techniques in Rapidly-Varied Unsteady Flows, 2004.

[23] D.H. Peregrine, Calculations of the development of an undular bore, J. Fluid Mech. 25 (1966) 321–330.

[24] S.B. Pope, Turbulent Flows, Cambridge University Press, 2000, p. 771.

[25] D. Reungoat, H. Chanson, B. Caplain, Sediment processes and flow reversal in the undular tidal bore of the Garonne River (France), Environ. Fluid Mech. 14 (3) (2014) 591–616, http://dx.doi.org/10.1007/s10652-013-9319-y.

[26] D. Reungoat, H. Chanson, C.E. Keevil, Field measurements of unsteady turbulence in a tidal bore: the Garonne River in October 2013, J. Hydraul. Res. 53 (3) (2015) 291–301, http://dx.doi.org/10.1080/00221686.2015.1021717, IAHR.

[27] H. Schlichting, Boundary-layer Theory, McGraw-Hill, New York, USA, 1979, 817 pages.

[28] B. Simon, Effects of Tidal Bores on Turbulent Mixing: a Numerical and Physical Study in Positive Surges Ph.D. thesis, School of Civil Engineering, The University of Queensland, Brisbane, Australia, 2014, 259 pages & 7 movies.

[29] B. Simon, H. Chanson, Turbulence Measurements in Tidal Bore-like Positive Surges over a Rough Bed Hydraulic Model Report No. CH90/12, School of Civil Engineering, The University of Queensland, Brisbane, Australia, 2013, 176 pages.

[30] M.R. Spiegel, Theory and Problems of Statistics, McGraw-Hill Inc., New York, USA, 1972.

[31] J.J. Stoker, Water Waves. The Mathematical Theory with Applications, Interscience Publishers, New York, USA, 1957, 567 pages.

[32] R.A.R. Tricker, Bores, Breakers, Waves and Wakes, American Elsevier Publ. Co., New York, USA, 1965.